Indian Journal of Pure & Applied Physics
Vol. 63, October 2025, pp. 924-929
DOI: 10.56042/ijpap.v63i10.19379

Atomic Magnetometer Based on Chip Scale Rb Atomic Vapour Cell

Giridhar M S*, Ishan Gunjal, Bhuvaneswari S, Kirankumar M, Brundana S D & S P Karanth
Laboratory for Electro-Optics Systems, Indian Space Research Organization, Bengaluru 560 058, India

Received: 3rd May 2025; accepted: 17th July 2025

This paper reports the development and characterization of an atomic magnetometer with a microfabricated Rb atomic vapour cell as the sensing element. The measurement principle is based on the Faraday rotation of linearly polarized probe light, which interacts resonantly with atomic spin states in the presence of a magnetic field. In the chip-scale vapour cell (dimensions: 8.0 mm × 12.0 mm × 1.5 mm), the atomic vapour is confined to a micromachined optical cavity of 3.5 µL with an optical path length of 0.5 mm. Optical interrogation is performed using a single laser beam tuned to the D1 absorption resonance of ^{85}Rb. The rotation arises due to magnetically induced circular birefringence in the hot atomic vapour. A bench model of the magnetometer is demonstrated over a measurement range of ±50 µT with a maximum uncertainty of 800 nT in an unshielded environment. The magneto-optic rotation (MOR) response in the laboratory was investigated and is observed to vary from 5×10³ rad/T for near zero magnetic field to 3.2×10³ rad/T for ambient geomagnetic field.

Keywords: Atomic magnetometer, Chip scale alkali vapour cell, Faraday rotation

1 Introduction

Precise magnetic field measurement is fundamental to a wide range of scientific, industrial, medical, and strategic applications. Over the past century, various types of magnetometers have been developed for specific use cases, employing a broad spectrum of physical phenomena. Some of these techniques have matured into high-sensitivity instruments widely adopted in the industry. Commonly used magnetometers are based on principles such as magnetoresistance, the Hall effect, and quantum effects in Superconducting Quantum Interference Devices (SQUIDs). These techniques involve measurements of induced voltages in pickup coils, magnetic saturation in materials, magneto resistive behaviour, Hall voltages, and Lorentz forces[1].

Recent advancements in solid-state lasers, optics, and micromachining have led to the development of optically pumped magnetometers (OPMs). OPMs leverage fundamental quantum properties of atoms, such as the interaction of polarized light with atomic spin states and selective excitation of atoms to magnetically sensitive energy levels.

High-sensitivity quantum magnetometers are in increasing demand for use in space, industrial, medical, and defence applications[2]. For space missions, these magnetometers provide low-SWaP (Size, Weight, and Power) solutions required by Earth observation satellites[3], deep-space missions[4], planetary fly-by probes, and rovers. In biomedical context, quantum magnetometers are used for real-time, high-spatial-resolution measurements of magnetic fields near the human scalp in the range of 1–10 pT. This technique, known as magnetoencephalography (MEG), is implemented using miniature OPM arrays embedded in lightweight helmets worn by patients[5].

The absolute nature of quantum magnetometers allows deployment in remote environments where recalibration is not feasible[6,7]. For attitude sensing in spacecraft, their drift-free performance eliminates the need for orientation manoeuvres typically required for calibration of conventional fluxgate magnetometers. Their low thermal drift also makes them well suited for strategic use in airborne, ground, or underwater platforms that experience wide temperature variations. Strategic applications include magnetic anomaly detection for unexploded ordnance (UXOs), landmines, and person-borne improvised explosive devices (IEDs) at large standoff distances, where field changes of just a few nanotesla must be detected against the Earth's ambient field[8,9].

We present the operating principle and test results of a bench-top atomic magnetometer designed for measuring the geomagnetic field, its local variations and anomalies therein. The system employs a

Corresponding author: E-mail: giri@leos.gov.in

single-beam interrogation of Rb atoms in vapor phase, confined in a 3.5 µL optical cavity within a micromachined chip-scale atomic vapor cell developed in-house. The cells were fabricated using well-established MEMS process technologies with batch production capabilities. The design and fabrication details is reported in our earlier work[10].

2 Principle of Operation

Magnetic field measurement is based on the magneto-optical rotation (MOR) of linearly polarized light due to magnetically induced circular birefringence in Rb atomic vapour. As the light passes through a magnetically sensitive birefringent medium, the anisotropy in the refractive indices for right- and left-circularly polarized components induces a rotation in the plane of polarization. This MOR is a function of the longitudinal component of the magnetic field, and is measured using a balanced polarimeter. Fig. 1 illustrates the principle of measurement of the atomic magnetometer.

The general expression for optical rotation (Φ) through a birefringent medium of length l is given in Eq. 1[11]

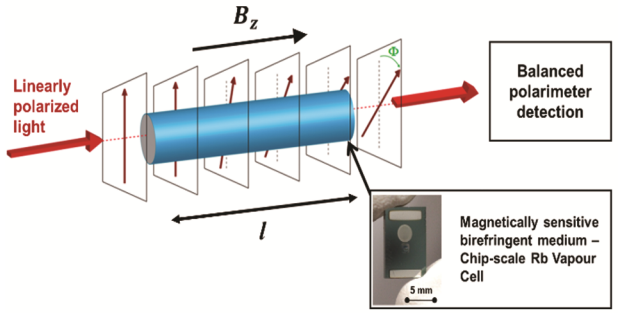

Fig. 1 — Principle of measurement of the atomic magnetometer

$$\Phi = \frac{\omega}{2c}\left(\int_0^l Re[n_+(\omega, B_z) - n_-(\omega, B_z)]\, dz\right) \quad \ldots (1)$$

where n_+ and n_- are the magnetically sensitive refractive indices for the right and left circularly polarized components of light, ω is the frequency of probe beam and c is the speed of light in vacuum and B_z is the magnetic field component along the light propagation.

Circular birefringence induced in Rb atomic vapour in the presence of a magnetic field is measured by the optical rotation of a linearly polarized light. Maximum rotation is observed when the incident light is tuned close to the absorption resonance. The MOR as a function of the longitudinal magnetic field can be approximated as[12, 13]

$$\Phi(B_z) \cong \frac{(2g_F\mu_B B_z/\hbar\Gamma)}{1+(2g_F\mu_B B_z/\hbar\Gamma)^2}\frac{l}{l_o} \quad \ldots (2)$$

where Φis the MOR, B_z is the magnetic field along the optical axis, g_F is the ground state electron Lande g factor, μ_B is the Bohr magneton, $\hbar$ is the Planck's constant, l is the optical cavity length, Γ is the relaxation rate and l_o is the absorption length.

Energy level diagram for the ^{85}Rb D1 transition is shown in Fig. 2 (a). The $F = 3 \rightarrow F'$ transition, used in this work, is indicated in the figure. Figure. 2 (b) shows the absorption spectrum obtained from the vapour cell containing natural Rb and the corresponding transitions are detailed in the inset. In the present work, the transition corresponding to $f = 377.10591\, THz$ is selected for its strong interaction with the interrogation beam.

3 Experimental

A functional block diagram of the experimental setup is shown in Fig. 3. Photograph showing the optics and the sensing module is shown in Fig. 4.

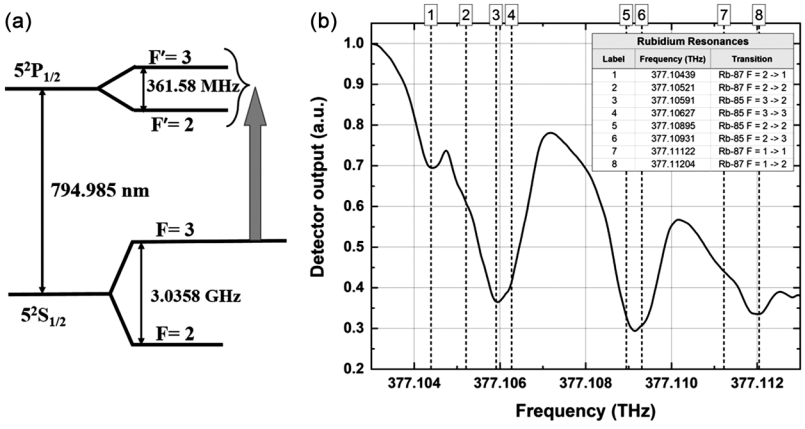

Fig. 2 — (a) ^{85}Rb energy level diagram for the D1 transition showing the hyperfine levels; and (b) Absorption spectrum from the vapour cell

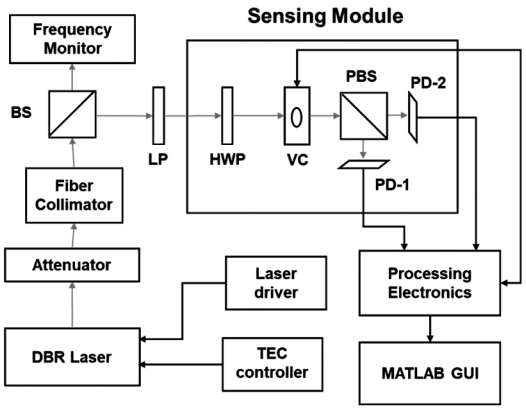

Fig. 3 — Functional block diagram of the experimental setup

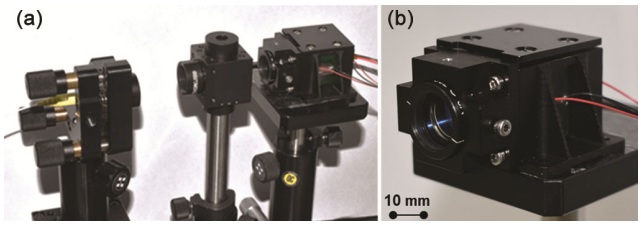

Fig. 4 — (a) the bench top magnetometer test setup. Pictured from left to right: fiber collimator, beam splitter, linear polarizer, magnetometer sensing module; and (b) Sensing module

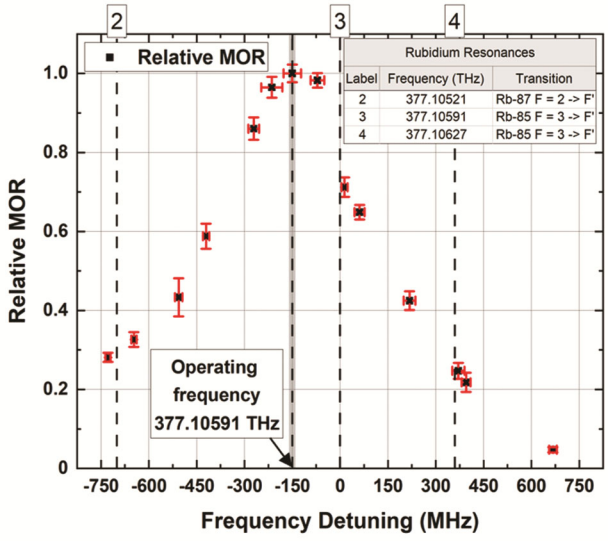

Fig. 5 — Dependence of MOR on laser frequency detuning

The light source is a Distributed Bragg Reflector (DBR) laser (Thorlabs DBR795PN) operating at 795 nm. Herein, a single beam is used for pumping and probing the atomic medium. The laser frequency was detuned with respect to the selected absorption resonance to obtain the maximum MOR. Figure 5 shows the MOR as a function of laser frequency detuning. A detuning of 150 MHz corresponding to a frequency of 377.10576 THz resulted in maximum MOR.

Laser temperature is stabilized to within ±5 mK using the built-in thermoelectric cooler (TEC) of the laser package. The temperature and injection current are controlled via bench top controllers (TEC200C and LDC205C respectively). Optical power is reduced to 200 µW using a variable fiber optic attenuator (Thorlabs VOAMMF). A fiber-coupled collimator generates a 2 mm diameter collimated beam. A fraction of the beam is diverted by a beam splitter to a wavelength meter for continuous monitoring of the laser frequency. In this configuration, ~100 µW of power is incident on the chip-scale vapour cell.

Following the beam splitter, a zero-order linear polarizer (LP) removes polarization noise due to mechanical or thermal perturbations in upstream optics. The transmission axis of the LP is aligned with that of the polarizing beam splitter (PBS) in the polarimeter. A half-wave plate (HWP) rotates the polarization by 45° with respect to the PBS axis. This configuration ensures a balanced polarimeter output in the absence of an external magnetic field. The desired polarization angle is achieved when the HWP's fast axis is at 22.5° relative to the LP.

The sensing module comprises a heater-integrated Rb vapour cell and a polarimeter. The polarimeter includes a PBS and two silicon PiN photodetectors (PD-1 and PD-2), which measure the vertical and horizontal polarizations. The resulting photocurrents are converted to voltages using two trans-impedance amplifiers (TIA). These signals are digitized by a 16-bit delta-sigma analog-to-digital converter (ADC) at a sampling rate of 20 Hz. A microcontroller interfaces with the ADC and streams the data to a MATLAB-based graphical user interface (GUI), which displays both raw detector counts and derived parameters in real time. The vapour cell is heated to 62 °C with a stability of 100 mK using a pulse-width modulation (PWM)-based controller. Transparent indium tin oxide (ITO) thin films (~200 nm) deposited on the vapour cell act as integrated heating elements. The photograph of the sensing module in Fig. 4 (b), weighs 35 grams with a total volume of 45 mm × 35 mm × 35 mm.

Before heating the vapour cell, the laser is switched on and the HWP is adjusted to equalize the power incident on both polarimeter channels to minimize the rotation offset.

The MOR is obtained from the polarimeter output using the following Equation:

$$\Phi = \frac{1}{2} sin^{-1}\left(\frac{I_V - I_H}{I_V + I_H}\right) \quad \ldots (3)$$

I_V and I_H represent the digital counts from the detectors corresponding to intensities of vertical and horizontal components emerging from the vapour cell.

Heating of the vapour cell is achieved by ITO film deposited directly onto the vapour cell. Considering the smaller path length of 0.5 mm, thermal gradient within the vapour cell is negligible. Further, experiments are carried out only after the vapour cell reaches stable temperature.

The sensitive axis of the magnetometer is defined by the direction of light propagation through the vapour cell. To minimize offset due to stray magnetic fields, the system is mounted on a movable wooden table, which can be rotated to align the optical axis toward geographic north within the laboratory.

4 Results and Discussions

The atomic magnetometer was calibrated against a reference magnetometer with a resolution of 0.1 nT with a dynamic range of ±100 μT (Nano Tesla Meter – RM100). A Helmholtz coil was used both to compensate for the ambient magnetic field and to apply known magnetic field over it. The applied field was varied from -70 μT to +70 μT, and the sensor's MOR response was recorded. The measured MOR as a function of the applied magnetic field is shown in Fig. 6.

To derive the magnetic field from measured MOR, the data was fitted using Equation (2), yielding the fitting parameters $\Gamma = 4.73\,MHz$ and $l/l_0 = 4 \times 10^4$. The equation with the extracted fit parameters is inverted to obtain the transfer function for the magnetometer. The measured field B_z as a function of MOR can be expressed as:

$$B_z(\Phi) \cong \frac{\hbar\Gamma}{2g_F\mu_B} \frac{(l/l_0) - \sqrt{(l/l_0)^2 - (2\Phi)^2}}{2\Phi} \quad \ldots (4)$$

Figure 7 shows the correlation between the magnetic field values measured by the two magnetometers. Across the ±50 μT range, the maximum deviation observed is less than 3 μT, corresponding to a measurement error less than 3%.

Stability and noise measurements were performed in three different orientations of the sensor's optical axis: 90° E, 75° NE, and 0° N. These orientations were chosen to expose the sensor to effective magnetic fields of about 0 μT, 10 μT, and 37.5 μT, respectively, in an unshielded condition. For each orientation, stability data was recorded for 600 s. The data, converted to magnetic field units using Eq. (4), is shown in Fig. 8.

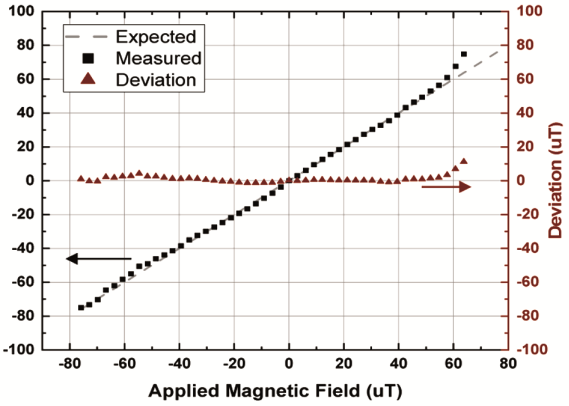

Fig. 7 — Correlation between the magnetic field measured by the reference magnetometer and the magnetometer presented in this work

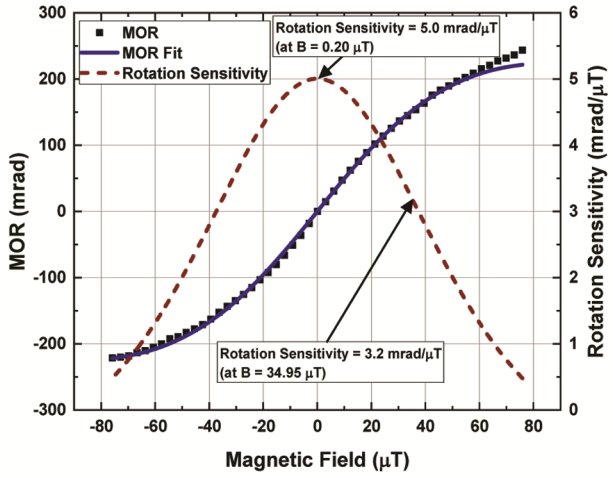

Fig. 6 — Response of the atomic magnetometer to the applied magnetic field. The solid black line represents the fit to Eq. (2)

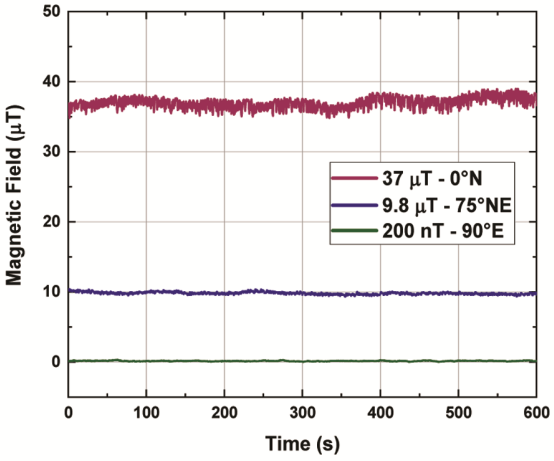

Fig. 8 — Stability plots of the magnetometer output for three different orientations in ambient geomagnetic field

Key parameters such as ambient magnetic field, measured MOR, standard deviation, MOR sensitivity, calculated field, and uncertainty are summarized in Table 1.

Since the final objective of this work is to develop a compact atomic magnetometer for field deployment, characterization was performed in the ambient geomagnetic field rather than in a magnetically shielded environment. To characterize the sensor's response to changes in the longitudinal component of the geomagnetic field, the magnetometer, assembled on a mobile wooden platform, was manually rotated through 360°. Figure 9 (a) shows a screenshot of the real-time MATLAB-based GUI displaying detector counts and derived MOR signals during the rotation. The rotation started from 180° S. At 270° W, the polarimeter signals became nearly balanced, and at 0° N, they were inverted. This indicates that the MOR vector crosses the optical axis. Continuing the rotation completes a full cycle, with the detector signals returning to their original values at 180° S.

The corresponding magnetic field output during this rotation is shown in Fig. 9 (b), where field values are plotted against the data index representing angular position.The performance of the developed atomic magnetometer is compared with similar chip scale atomic magnetometer reported for geomagnetic field studies on either terrestrial or low earth orbit (LEO) platforms[14-19]. Table 2 presents the comparison of atomic species, optical interrogation length, operating range, bandwidth, sensitivity (noise floor) or measurements uncertainty and operating conditions. As the developed magnetometer was meant for field deployment and geomagnetic field studies, the sensitivity reported herein is measured in ambient conditions unlike the reported sensitivities which were measured in shielded condition.

Table 1 — Key parameters measured by the magnetometer for three different orientations in ambient geomagnetic field

Optical axis	90° E	75° NE	0° N
Ambient magnetic field (μT)	0	10	37.5
MOR (mrad)	1.02	8.65	158.46
MOR standard deviation (mrad)	0.294	0.840	2.46
MOR response (mrad/μT)	5	4.8	3.2.
Measured magnetic field (μT)	0.2	9.8	37
Measurement uncertainty (nT)	58.7	174	811

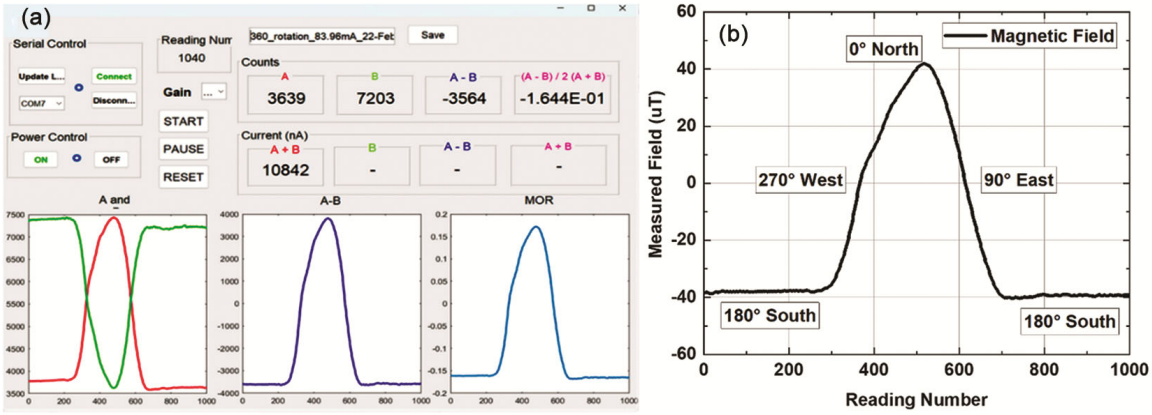

Fig. 9 — (a) Real-time sensor response for 360° rotation; and (b) Output of the magnetometer in field units over the full rotation

Table 2 — Performance comparison of developed atomic magnetometer

Atomic species	Rb optical cavity length (Interrogation length)	Operating range	Band width	Sensitivity / Uncertainty	Operating conditions	Reference
^{87}Rb	1.0 mm	40 μT to 50 μT	10 Hz	630 nT	TRICE-2 sounding rocket mission close to north pole	[14]
^{87}Rb	1.0 mm	20 μT to 70 μT	1 Hz	5 nT	COSMO CubeSAT LEO mission (Proposed)	[15]
^{133}Cs	4.0 mm	± 50 μT	450 Hz	10 pT/√Hz	Unshielded geomagnetic environment	[16]
^{87}Rb	1.5 mm	~ 31 μT	300 Hz	40 pT/√Hz	Unshielded geomagnetic environment	[17]
Natural Rb	1.3 mm	20 -100 μT	1 Hz	200 pT/√Hz	Unshielded geomagnetic environment	[18]
Natural Rb	4.0 mm	± 10 μT	100 Hz	700 pT/√Hz	Unshielded with Helmholtz coils	[19]
Natural Rb	0.5 mm	± 50 μT	10 Hz	20 nT/√Hz	Unshielded with Helmholtz coils	This work

5 Conclusion

This work reports the principle of operation and experimental results of a bench-top atomic magnetometer based on a micro fabricated, chip-scale Rb atomic vapour cell with an interrogation volume of 3.5 µL. The calibration methodology, stability analysis, and the sensor's response to the ambient geomagnetic field under laboratory conditions have been presented.

The magnetometer demonstrates a measurement range of ±50 µT, with an uncertainty of 800 nT at the extremes and 58 nT near zero field. Further, the measurements from the developed atomic magnetometer are validated against the field measured by a standard reference magnetometer and it was found that the deviation is less than 3%.

All measurements and characterizations were carried out in an unshielded environment, highlighting thesensor's robustness in practical conditions. The current bench-top design is being further refined to improve optical alignment, laser frequency stabilization, and thermal control, with the goal of enhancing the overall sensor performance. A compact, packaged version with integrated processing electronics is under development for space deployment, and its performance will be reported in future publications.

References

1 Grosz A, Haji-Sheikh M & Mukhopadhyay, S C, *Springer International Publishing* (2016).

2 Bai X, Wen K, Peng D, Liu S & Luo L, *Front Phys* 11 (2023) 1212368.

3 Zhou B, Cheng B, Gou X, Li L, Zhang Y, Wang J, Magnes W, Lammegger R, Pollinger A, Ellmeier M, Xiao Q, Zhu X, Yuan S, Yang Y & Shen X, *Earth Planets Space*, 71 (2019) 119.

4 Amtmann C, Pollinger A, Ellmeier M, Dougherty M, Brown P, Lammegger R, Betzler A, Agú M, Hagen C, Jernej I, Wilfinger J, Baughen R, Strickland A & Magnes W, *GeosciInstrum Method Data Syst*, 13 (2024) 177.

5 BrookesM J, Leggett J, Rea M, Hill R M, Holmes N, Boto E & Bowtell R, *Trends Neurosci*, 45 (2022) 8.

6 Marcin M, Angus B, Paul G, Dominic H, David B, James P M, Erling R, Ciarán B & Stuart I, *Sci Rep,* 14 (2024) 28229.

7 Levi K, Giat A, Golan L, Talker E & Stern L, *Optica Quantum*, 3 (2025) 84.

8 Gregory S, Jonathan M & Vishal S, *Defense Technical Information Center*, ADA584867 (2012) 2.

9 Yoo L-S, Lee J-H, Lee Y-K, Jung S-K & Choi Y, *Sensors*, 21 (2021) 3175.

10 GiridharM S, NandakishorM M, Dahake A, Tiwari P, Jambhalikar A, John J & Karanth S P, *ISSS J Micro Smart Syst*, 11 (2022) 427.

11 Budker D & Kimball D J, *Optical Magnetometry Cambridge University Press* (2013).

12 Vineeth Francis T J, Suna R R, Madhu P K, Viswanathan N K & Rajalakshmi G, *AIP Advances*, 9 (2019) 065113.

13 Kurian G, Sahoo S S, Madhu P K & Rajalakshmi G, *Phys Rev Appl*, 19 (2023) 054040.

14 Korth H, Kitching J E, Bonnell J W, Bryce B A, Clark G B, Edens W K, Gardner C B, Rachelson W & Slagle A, *Rev SciInstrum*, 94 (2023) 035002.

15 Ellmeier M, Jim´enez-Mart´ınez R, Allison D, Maydew T, Hughes J, Chism C, Marshall R, Alem O & Knappe S. *Proc. SPIE 13392, Quantum Sensing, Imaging, and Precision Metrology III,* (2025) 133920A.

16 Oelsner G, Jsselsteijn R, Scholtes T, Krüger A, Schultze V, Seyffert G, Werner G, Jäger M, Chwala A & Stolz R, *Phys Rev Appl*, 17 (2022) 024034.

17 Levi K, Giat A, Golan L, Talker E & Stern L, *Optica Quantum,* 3 (1) (2025) 84.

18 Pan Z, Shang J, Lu L & Ji Y, *Proceedings of the IEEE 18th International Conference on Electronic Packaging Technology* (2017).

19 Sebbag Y, Talker E, Naiman A, Barash Y & Levy U, *Light: Sci Appl*, 10 (2021) 54.